Cong *et al.*
EURASIP Journal on Advances in Signal Processing (2022) 2022:12
https://doi.org/10.1186/s13634-022-00849-4

EURASIP Journal on Advances in Signal Processing

RESEARCH Open Access

Range-Doppler domain spatial alignment for networked radars

Xiaoyu Cong, Yubing Han*, Weixing Sheng, Shanhong Guo and Hui Sun

*Correspondence:
hanyb@njust.edu.cn
School of Electronic and Optical Engineering, Nanjing University of Science and Technology, Nanjing 210094, China

Abstract

An important prerequisite for the radar network detection is that the measurements from local radars are transformed to a common reference frame without systematic or registration errors. For the signal level alignment, only partial signals are available for global decision-making due to power and bandwidth limitations. In this paper, a low-communication-rate spatial alignment in range-Doppler domain is proposed for networked radars without the prior spatial information (positions and attitudes) of radars, which is different from the existing methods in the trajectory domain or echo domain for alignment. To reduce the radar-to-fusion-center communication-rate, the method of initial constant false alarm rate detection is used to censor the signals in range-Doppler domain from local radars. Based on the spatial alignment model for the networked radars in geometry, a maximization problem is formulated. The objective function is the cross-correlation between the range-Doppler domain signals from different local radars. The optimization problem is solved by a genetic algorithm. Simulation results show that the rotation matrix and translation vector are estimated, and the detection probability of the proposed algorithm is improved after alignment and fusion compared with state-of-art methods.

Keywords: Spatial alignment, Networked radars, Low communication rate, Range-Doppler domain, Genetic algorithm

1 Introduction

Networked radars can share different views of data from multiple stand-alone radars for fusion so as to improve the target tracking accuracy. The information fusion of multiple radars has the advantages of increasing the surveillance systems accuracy and enhancing the reliability [1–4].

Before fusion, the data measured by local radars should be transformed to a common spatial coordinate system to acquire the reliable information of targets [5]. However, due to the deviation and measurement errors of radars, it is difficult to ensure the accuracy for tracking. Therefore, a significant prerequisite for successful integration of networked radars is the spatial alignment [6].

Previously proposed alignment methods for networked sensors fall into two classes. The first class formulates alignment model based on target trajectories from local radars. The Kalman filter (KF) alignment algorithm [7] was used to estimate sensor

deviation parameters, and extended Kalman filter (EKF) [8], unscented Kalman filter (UKF) [9], sparse-grid quadrature Kalman filtering (SGQKF) [10] alignment were proposed for nonlinear models. A linear least squares (LS) estimator of bias terms was derived in [11], where the registration errors including attitudes, measurements, and position biases were all considered. The attitudes here mean attitude (orientation) angles. The attitude angles include three angles: the yaw angle, pitch angle and roll angle. Based on LS registration, an exact least square (ELS) registration [12] was presented to correct the systematic errors for networked dissimilar sensors, and a recursive two-step optimization algorithm was proposed to estimate both the target state and sensor bias. A maximum likelihood registration (MLR) algorithm [13] was proposed for the spatial alignment of multiple possibly dissimilar sensors, which output estimates of the registration parameters, registered sensor measurements and target locations. A distributed probability hypothesis density (PHD) filter for on-line joint sensor registration [14] was presented for multi-target tracking by Doppler radars. An alignment algorithm which registered asynchronous measurements from networked radars was proposed in [15], where the positions, attitudes and delays of radars were not required. In recent years, with the development of deep learning technology, the alignment parameter estimations based on neural networks [16, 17] have been proposed for networked radars.

The second class performs alignment in the signal level. The existing alignment algorithm in the signal level transmits target echoes to the fusion center for comprehensive processing, which takes full advantage of the echo information. A signal-domain alignment algorithm for SAR was proposed in [18], which performed registration in the pre-processing stage, i.e., in the target echo. Pulse correlation was used to align the corresponding pulses and to correct the time delay. An alignment method based on signal-domain Kalman filtering was presented in [19]. A Bayes based method was derived to jointly estimate the range and DOA errors by comparing the reference signal and return signal, and a precise measurement model for motion variables was constructed to realize tracking combined with Kalman filter. To overcome the target detection problem with registration errors in multistatic radar, a maximum likelihood estimation-based generalized likelihood ratio test (ML-GLRT) detector and a maximum a posteriori estimation-based generalized likelihood ratio test (MAP-GLRT) detector were proposed in [20]. Considering the influence of interference on target detection, the Rao and Wald tests for subspace target detection were proposed in the presence of three cases of coherent interference, namely, known interference, partially known interference, and completely unknown interference [21]. A three-dimensional (3D) reconstruction algorithm was proposed for multistatic ISAR systems [22], and the target 3D geometry can be obtained by solving the projection equations between the target 3D geometry and ISAR images. In [23], a multi-dimensional signal model was established including the parameters on the target 3-D position, translation velocity, and rotating angular velocity. A gridless method based on atomic norm optimization and the pairing correction were proposed to remove registration errors and improve the accuracy. However, the aforementioned algorithms align the target echo directly and usually require each radar station to transmit all the received signals to the fusion center for alignment, which requires a high-communication-rate.

In addition, the signal submerged in noise reduces the accuracy of alignment in case of low SNR. Moreover, prior spatial information (including locations and attitudes of radar stations) are required.

Using the alignment method based on target trajectories (the first class), it is only required to transmit the target trajectories measured by local radars to the fusion center, and then the spatial alignment parameters can be estimated from the comprehensive processing by the fusion center. The advantage of such an approach is that the communication-rate between the local radar and the fusion center is low. However, since only the data in the trajectory level is used, a lot of echo information is discarded, which reduces the accuracy of the spatial alignment. Conversely, the alignment algorithm in the signal level (the second class) makes the best use of echo information, and the accuracy of the spatial registration for networked radars is improved. Accordingly, the required communication-rate increases substantially. The existing alignment in the signal level uses the echo signal from multiple radars, and the alignment in the trajectory level uses the target trajectory. The echo signal contains more informative data, therefore, the accuracy of the alignment in the signal level is higher compared with that in the trajectory level. However, the amount of the data transmission is too large if the whole echo is used in the alignment algorithm of the signal level. Only partial signals in the echo are available for global decision-making due to power and bandwidth limitations. Therefore, the censoring method of the data is important. If the censoring method is unreasonable and too much target information in the echo is lost, the accuracy of the alignment in the signal level will be reduced. Some quantitative fusion and censoring sensors algorithms [24–26] have been proposed to reduce the communication-rate between the local radars and fusion center. However, these low-communication-rate algorithms are discussed in the condition that the data have been aligned exactly (i.e. there are no registration errors). Therefore, these algorithms are not applicable to the transmission for unaligned signals.

In this paper, a low-communication-rate algorithm is proposed to estimate the spatial alignment parameters for networked radars in range-Doppler domain. Multiple radars preprocess the echoes received by the antenna and obtain their respective signals after moving target detection (MTD). The signal in range-Doppler domain is used for alignment, which is different from the existing alignment of the echo signal. In order to reduce the radar-to-fusion-center communication-rate, initial constant false alarm rate (CFAR) detection is used to censor the informative data in range-Doppler domain from local radars. The parameters to be estimated for the spatial alignment include the rotation matrix and translation vector. Based on the alignment model in geometry, a maximization problem is formulated. The objective function is the cross-correlation between the range-Doppler domain signals from different local radars. The optimization problem can be solved by a genetic algorithm (GA) to estimate the rotation matrix and translation vector. The technical contributions of this paper are summarized below:

1. A spatial alignment algorithm in range-Doppler domain is proposed for networked radars without the prior information including positions and attitudes of local radars, which is different from the existing methods in trajectory or echo domain for alignment and improves the alignment accuracy.

2. Before transmission, the signals in range-Doppler domain are censored by initial CFAR detection. Only data that exceed the threshold are transmitted to the fusion center for alignment, which greatly reduces the communication-rate.
3. The objective function is established symmetrically, that is, local radars are respectively used as the reference radar for alignment, which improves the accuracy for alignment.

The rest of the paper is organized as follows. Section 2 proposes the alignment problem formulation in range-Doppler domain. The spatial alignment algorithm in range-Doppler domain for networked radars is presented in Sect. 3. Section 4 provides experimental results. Section 5 gives conclusions.

2 Problem formulation

The signal processing and fusion model for networked radars is shown in Fig. 1. Two radars are considered as examples without loss of generality.

A linear frequency modulation (LFM) signal is selected as the detection signal for networked radars. We assume that each coherent processing interval (CPI) contains N pulse repetition intervals (PRIs), and the n-th transmitted pulse from radar A can be expressed as

$$s_{\mathrm{A},0}\left(t_n,\tilde{t}\right)=a_0\left\{\mathrm{rect}\left(\frac{\tilde{t}}{T_p}\right)\exp\left[j2\pi\left(f_c\left(t_n+\tilde{t}\right)+\frac{1}{2}\mu\tilde{t}^2\right)\right]\right\}, \tag{1}$$

where a_0 is the amplitude of transmitted signals, T_p is the pulse width, T_r is the pulse repetition interval, f_c is the carrier frequency, $\mu=\frac{B}{T_p}$ is the chirp rate, B is the bandwidth of the LFM signal, $\mathrm{rect}(x)=\begin{cases}1 & 0<x<1\\ 0 & \text{else}\end{cases}$, n is the index of the transmitted pulse , $t_n=nT_r$ is the slow time, $\tilde{t}$ is the fast time. After down-conversion and digital beam forming (DBF) in the receiver, the echo can be represented as

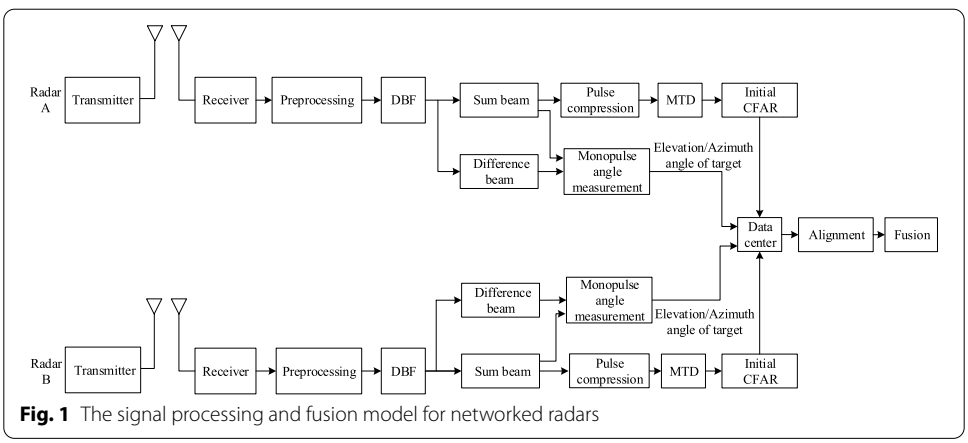

Fig. 1 The signal processing and fusion model for networked radars

$$s_{\mathrm{A,r}}(t_n,\tilde{t}) = G_{\mathrm{A}}K_{\mathrm{A}}(t_n,\tilde{t})\left\{\mathrm{rect}\left(\frac{\tilde{t}-\tau_{\mathrm{A}}(t_n,\tilde{t})}{T_p}\right)\cdot \exp\left[j2\pi\left(f_{\mathrm{A,d}}(\tilde{t}+t_n)+\frac{1}{2}\mu(\tilde{t}-\tau_{\mathrm{A}}(t_n,\tilde{t}))^2-f_c\tau_{\mathrm{A}}(t_n,\tilde{t})\right)\right]\right\}+w_{\mathrm{A}}(t_n,\tilde{t}) \tag{2}$$

where G_{A} is the antenna gain, $K_{\mathrm{A}}(t_n,\tilde{t})$ is the amplitude of the echo signal, $\tau_{\mathrm{A}}(t_n,\tilde{t}) = \frac{2(R_{\mathrm{A}}(t_n)+v_{\mathrm{A}}\tilde{t})}{c}$ is the delay of the target at time $(t_n,\tilde{t})$, $R_{\mathrm{A}}(t_n)$ is the range between radar A and the target at time t_n, v_{A} denotes the radial velocity of the target to radar A, $f_{\mathrm{A,d}} = \frac{2v_{\mathrm{A}}}{\lambda}$ is the Doppler frequency, $\lambda = \frac{f_c}{c}$ is the wave length, c is the electromagnetic wave velocity, $w_{\mathrm{A}}(t_n,\tilde{t})$ is complex white Gaussian noise. Pulse compression is performed for each PRI of the echo, and the n-th pulse after pulse compression can be represented as

$$s_{\mathrm{A,c}}(t_n,\tilde{t}) = s_{\mathrm{A,r}}(t_n,\tilde{t}) \otimes h(\tilde{t}), \tag{3}$$

where $h(t)$ is the pulse response of the pulse compression filter, and $\otimes$ is convolution. To suppress spectrum leakage, Hamming Window w_h is added to the filter, therefore $h(\tilde{t})$ can be expressed as

$$h(\tilde{t}) = w_h(\tilde{t})\exp\left(j2\pi\left(-\frac{1}{2}\mu\tilde{t}^2\right)\right). \tag{4}$$

In order to suppress clutter, moving target detection (MTD) [27] is performed for the signals in (3), and the spectral lines of moving targets are filtered using a Doppler filter bank. Generally, fast Fourier transform (FFT) is used to realize the Doppler filter bank. After MTD, the echo is transformed to the signal in range-Doppler domain. Compared with the echo signal, the signals in range-Doppler domain are accumulates in the frequency domain, which is convenient to extract the target information in low SNRs. Since the complex signals received by different radars are non-coherent, the absolute values of signals after MTD are measured for alignment. The measurements in range-Doppler domain can be represented as

$$s_{\mathrm{A,m}}(t_n,\tilde{t}) = \left|\sum_{i=1}^{N} s_{\mathrm{A,c}}(t_i,\tilde{t})e^{-j2\pi ni/N}\right|, n = 1,2,3,...,N \tag{5}$$

In a pulse, $\tilde{t} = \frac{1}{f_s},\frac{2}{f_s},\frac{3}{f_s},..T_r$, where f_s is the sample rate. An $N \times M$ matrix $\mathbf{S}$ with K CPIs, which denotes the signal after MTD, is shown in Fig. 2, where $M = f_s T_r$. After MTD, the signals from radar A in range-Doppler domain can be represented as $\mathbf{S}^k_{\mathrm{A,m}}$ in the k-th CPI (Similarly, the signals from radar B in range-Doppler domain are $\mathbf{S}^k_{\mathrm{B,m}}$). The range and radial velocity of the target to radar A is different from those to radar B. Therefore, the signals $\mathbf{S}^k_{\mathrm{A,m}}$ and $\mathbf{S}^k_{\mathrm{B,m}}$ in range-Doppler domain should be aligned before fusion.

3 Proposed method

3.1 Spatial alignment model

The spatial relation in geometry between radars A and B is shown in Fig. 3. The position vectors of the target in A and B coordinate system for the kth CPI can be expressed as $\mathbf{P}^k = \left[x^k_{\mathrm{A}}, y^k_{\mathrm{A}}, z^k_{\mathrm{A}}\right]^{\mathrm{T}}$ and $\mathbf{Q}^k = \left[x^k_{\mathrm{B}}, y^k_{\mathrm{B}}, z^k_{\mathrm{B}}\right]^{\mathrm{T}}$, respectively, where the superscript T denotes

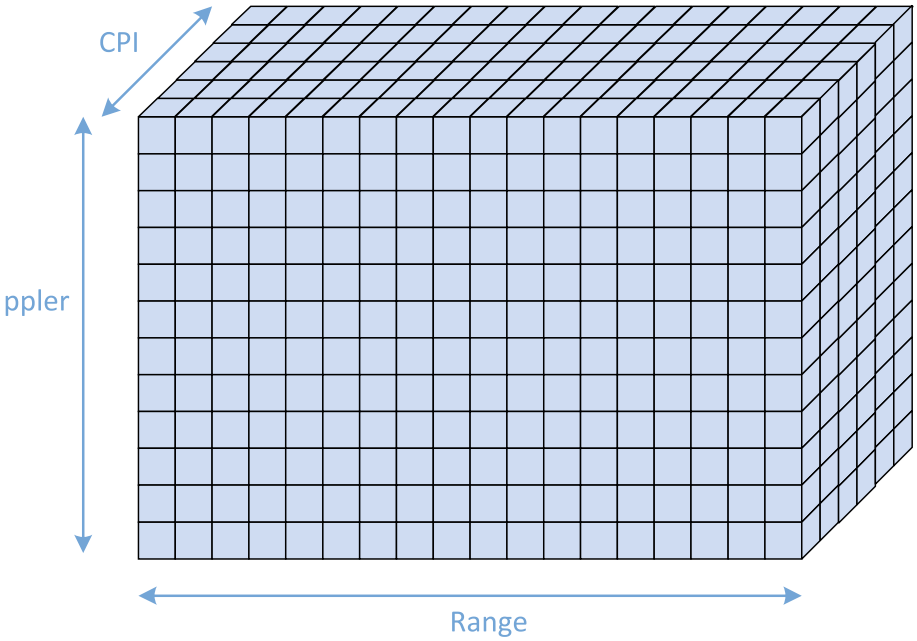

Fig. 2 Signal data after MTD

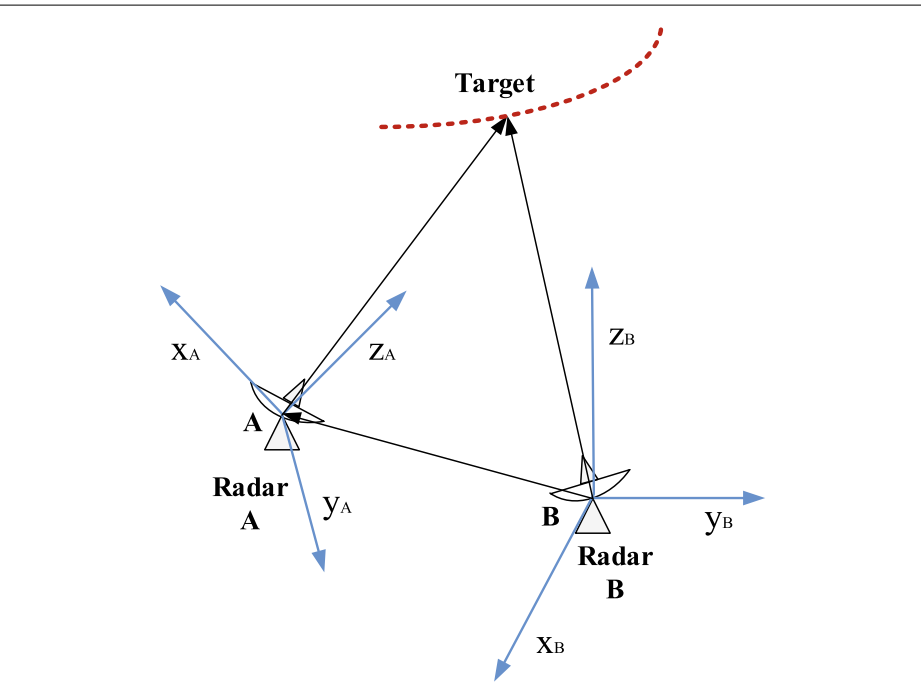

Fig. 3 The alignment model for networked radars

the transpose. It is worth stressing that, in this work, **P** and **Q** refer to the position vectors in Cartesian coordinates, while the measurements from radars refer to the positions in spherical coordinates. The geometrical convention for the Cartesian coordinate

system is that X axis is aligned with the East, Y axis with the North, and Z points upwards, which is called local Cartesian coordinate. For the spherical coordinates, we have that the azimuth φ is positive counter-clockwise from the East (X axis) and the elevation θ is positive counter-clockwise from the X − Y plane. From the geometry of the problem shown in Fig. 3, the following relation holds

$$\mathbf{P}^k = \mathbf{H}\mathbf{Q}^k + \mathbf{r}, \tag{6}$$

where $\mathbf{H}$ is 3×3 the rotation matrix of angles α, β, γ that aligns the radar B reference frame to the radar A reference frame. The rotation matrix $\mathbf{H}$ is given by

$$\mathbf{H} = \begin{bmatrix} \cos\alpha\cos\beta & \cos\alpha\sin\beta\sin\gamma - \sin\alpha\cos\gamma & \cos\alpha\sin\beta\cos\gamma + \sin\alpha\sin\gamma \\ \sin\alpha\cos\beta & \sin\alpha\sin\beta\sin\gamma + \cos\alpha\cos\gamma & \sin\alpha\sin\beta\cos\gamma - \cos\alpha\sin\gamma \\ -\sin\beta & \cos\beta\sin\gamma & \cos\beta\cos\gamma \end{bmatrix}. \tag{7}$$

In (6), $\mathbf{r}$ is 3×1 the translation vector expressed as $\mathbf{r} = \left[r_x, r_y, r_z\right]^{\mathrm{T}}$. The spherical-to-Cartesian transformation can be expressed as

$$\mathbf{P}^k = \begin{bmatrix} \rho_{\mathrm{A}}^k \cos\theta_{\mathrm{A}}^k \cos\varphi_{\mathrm{A}}^k \\ \rho_{\mathrm{A}}^k \cos\theta_{\mathrm{A}}^k \sin\varphi_{\mathrm{A}}^k \\ \rho_{\mathrm{A}}^k \sin\theta_{\mathrm{A}}^k \end{bmatrix}, \mathbf{Q}^k = \begin{bmatrix} \rho_{\mathrm{B}}^k \cos\theta_{\mathrm{B}}^k \cos\varphi_{\mathrm{B}}^k \\ \rho_{\mathrm{B}}^k \cos\theta_{\mathrm{B}}^k \sin\varphi_{\mathrm{B}}^k \\ \rho_{\mathrm{B}}^k \sin\theta_{\mathrm{B}}^k \end{bmatrix}, \tag{8}$$

where $\rho_{\mathrm{A}}^k, \theta_{\mathrm{A}}^k, \varphi_{\mathrm{A}}^k$ are the range, elevation angle and azimuth angle of the target to radar A, respectively, and $\rho_{\mathrm{B}}^k, \theta_{\mathrm{B}}^k, \varphi_{\mathrm{B}}^k$ are the range, elevation angle and azimuth angle of the target to radar B, respectively. The ranges and radial velocities of the target to radars A and B can be expressed as

$$\rho_{\mathrm{A}}^k = p_{\mathrm{A}}^k \Delta R_{\mathrm{A}}, \rho_{\mathrm{B}}^k = p_{\mathrm{B}}^k \Delta R_{\mathrm{B}}, \tag{9}$$

$$v_{\mathrm{A}}^k = q_{\mathrm{A}}^k \Delta d_{\mathrm{A}}, v_{\mathrm{B}}^k = q_{\mathrm{B}}^k \Delta d_{\mathrm{B}}, \tag{10}$$

where v_{A}^k and v_{B}^k are the radial velocities of the target to radars A and B, ΔR_{A} and ΔR_{B} are the range resolution cells, Δd_{A} and Δd_{B} are velocity resolution cells, p_{A}^k and q_{A}^k are the indexes of the cell in range-Doppler domain for radar A, p_{B}^k and q_{B}^k are the indexes of the cell in range-Doppler domain for radar B. By making use of (6), (8) and (9), the alignment for the range dimension can be expressed as

$$p_{\mathrm{B}}^k = \frac{1}{\Delta R_{\mathrm{B}}} \left(\mathbf{H} \begin{bmatrix} \cos\theta_{\mathrm{B}}^k \cos\varphi_{\mathrm{B}}^k \\ \cos\theta_{\mathrm{B}}^k \sin\varphi_{\mathrm{B}}^k \\ \sin\theta_{\mathrm{B}}^k \end{bmatrix} \right)^{+} \left(\Delta R_{\mathrm{A}} p_{\mathrm{A}}^k \begin{bmatrix} \cos\theta_{\mathrm{A}}^k \cos\varphi_{\mathrm{A}}^k \\ \cos\theta_{\mathrm{A}}^k \sin\varphi_{\mathrm{A}}^k \\ \sin\theta_{\mathrm{A}}^k \end{bmatrix} - \mathbf{r} \right), \tag{11}$$

where the superscript $+$ denotes the generalized inverse. The Doppler measured by radars A and B has a different mapping in different CPI. The radial velocities of the target to radars A and B in geometry are shown in Fig. 4.

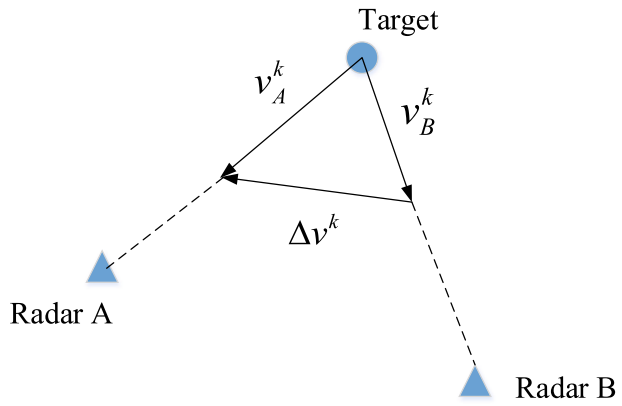

Fig. 4 The target Doppler from radars A and B

The alignment for Doppler dimension can be expressed as

$$q_{\mathrm{B}}^k = q_{\mathrm{A}}^k - \Delta q^k, \tag{12}$$

where $\Delta q^k = v_{\mathrm{A}}^k/\Delta d_{\mathrm{A}} - v_{\mathrm{B}}^k/\Delta d_{\mathrm{B}}$. Based on the range and velocity relations between radars A and B, the alignment equation between the index $\left(D_{\mathrm{A}}^k(i), R_{\mathrm{A}}^k(i)\right)$ of the target signal from radar A and $\left(X_{\mathrm{B}}^k(i), Y_{\mathrm{B}}^k(i)\right)$ from radar B in range-Doppler domain can be modeled as

$$\begin{aligned}&\left(X_{\mathrm{B}}^k(i), Y_{\mathrm{B}}^k(i)\right) = \\ &\left(D_{\mathrm{A}}^k(i) - \Delta q^k, \frac{1}{\Delta R_{\mathrm{B}}}\left(\mathbf{H}\begin{bmatrix}\cos\theta_{\mathrm{B}}^k\cos\varphi_{\mathrm{B}}^k\\ \cos\theta_{\mathrm{B}}^k\sin\varphi_{\mathrm{B}}^k\\ \sin\theta_{\mathrm{B}}^k\end{bmatrix}\right)^{+}\left(\Delta R_{\mathrm{A}}R_{\mathrm{A}}^k(i)\begin{bmatrix}\cos\theta_{\mathrm{A}}^k\cos\varphi_{\mathrm{A}}^k\\ \cos\theta_{\mathrm{A}}^k\sin\varphi_{\mathrm{A}}^k\\ \sin\theta_{\mathrm{A}}^k\end{bmatrix} - \mathbf{r}\right)\right).\end{aligned} \tag{13}$$

Equation (13) is the fundamental alignment equation in range-Doppler domain, which allows us to align signals coming from radar B to radar A. In the alignment model, (α, β, γ) in $\mathbf{H}$ and (r_x, r_y, r_z) in $\mathbf{r}$ are the unknown parameters to be estimated.

3.2 Range-Doppler domain spatial alignment

In this subsection, the signals in range-Doppler domain are aligned based on the spatial alignment equation above. In the radar network, the energy consumption and communication requirements are increased when local radars transmit all the data to the fusion center. Thus, when energy or communication resources are limited, we need to minimize the data transmissions between the local radars and the fusion center [24]. The two-step detection scheme is presented when a communication-rate restriction is imposed on a distributed radar network [26]. One approach to restricting the communication-rate is to initially censor. The initial threshold is set at each local radar, and only the data

that pass the initial threshold test are shared. The initial threshold test is considered as Stage 1 (first-stage detection) of the two-step detection scheme. After being censored, the data are transmitted to Stage 2 (second-stage detection) of the two-step detection scheme where they are integrated and compared to a final threshold corresponding to the desired overall probability of false alarm.

With the inspiration of the two-step detection scheme, initial CFAR as Stage 1 is carried out for the signal in range-Doppler domain to reduce the communication rate for alignment. The first-stage false alarm rate can be denoted as P_{fa1}, and T_1 is the first-stage threshold associated with P_{fa1}. In this paper, we use cell averaging false alarm rate (CA-CFAR) detector. Therefore, $T_1 = \left(\sum_{i=1}^{N_c} x_i\right)\left({P_{fa1}}^{-\frac{1}{N_c}} - 1\right)$, where x_i is the signal in the i-th cell and N_c is the number of reference cells. Only the cells that exceed the threshold T_1 are sent to the fusion center, and cells below the threshold T_1 is uninformative and simply not transmitted. In consideration of the situation that the strong signals raise the threshold of the surrounding cells, the weak signals near the strong signals may be undetected. In order to retain the weak signal, the cells around the signals that pass the threshold test are sent to the fusion center together. In this way, the radars censor their observations so that each radar only sends informative observations to the fusion center, and discards those uninformative data.

The informative cells in the kth CPI are censored and transmitted to the fusion center to prepare for the following alignment, as shown in Fig. 5. We select a $W \times G$ data set around the cell that passes the initial CFAR detection.

After the initial CFAR, the informative cells in range-Doppler domain are shown in Fig. 6. In this way, the information of the target can be retained to the greatest extent. Moreover, the communication-rate between local radars and the fusion center can be reduced.

The measurements $\mathbf{\Omega}^k_{\mathrm{A,m}}$ and $\mathbf{\Omega}^k_{\mathrm{B,m}}$ after the initial CFAR from radars A and B in the kth CPI can be denoted as

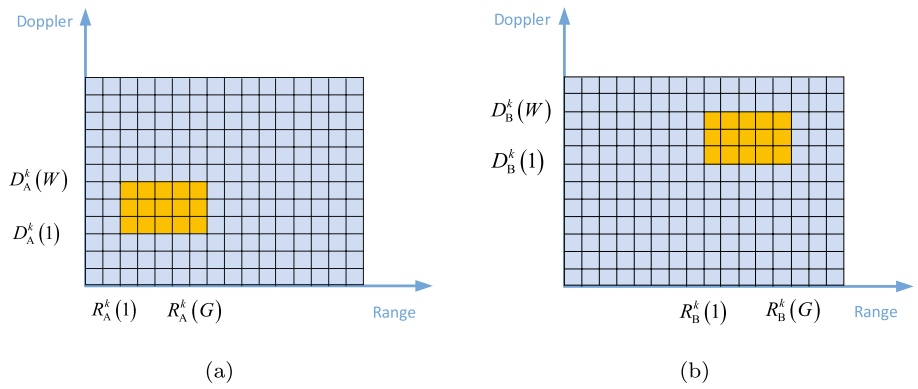

Fig. 5 A schematic diagram of censoring data using initial CFAR detection **a** signals after MTD from radar A in the k-th CPI **b** signals after MTD from radar B in the k-th CPI: The blue cells represent all the data after MTD. The yellow cells represent the data after the initial CFAR. For radar A, $R^k_{\mathrm{A}}(1)$, $R^k_{\mathrm{A}}(G)$ are the starting and ending indexes of censored cells in range dimension, and $D^k_{\mathrm{A}}(1)$, $D^k_{\mathrm{A}}(W)$ are the starting and ending indexes in Doppler dimension. For radar B, $R^k_{\mathrm{B}}(1)$, $R^k_{\mathrm{B}}(G)$ are the starting and ending indexes of censored cells in range dimension, and $D^k_{\mathrm{B}}(1)$, $D^k_{\mathrm{B}}(W)$ are the starting and ending indexes in Doppler dimension

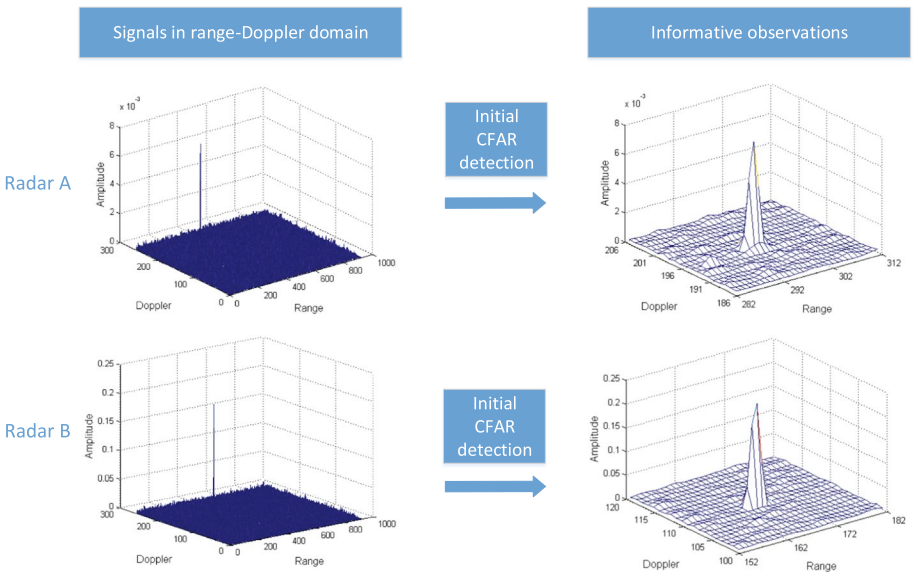

Fig. 6 Data censor for the signals in range-Doppler domain

$$\mathbf{\Omega}^k_{\mathrm{A,m}} = (\mathbf{F}_{\mathrm{A}})^{\mathrm{T}} \mathbf{S}^k_{\mathrm{A,m}} \mathbf{E}_{\mathrm{A}}, \tag{14}$$

where $\mathbf{F}_{\mathrm{A}} = \left[\mathbf{f}_{D^k_{\mathrm{A}}(1)} \ \mathbf{f}_{D^k_{\mathrm{A}}(2)} \ \cdots \ \mathbf{f}_{D^k_{\mathrm{A}}(W)} \right]$, $\mathbf{f}_{D^k_{\mathrm{A}}(i)} = \left[\mathbf{0}_{D^k_{\mathrm{A}}(i)} \ 1 \ \mathbf{0}_{M-D^k_{\mathrm{A}}(i)} \right]$, $\mathbf{E}_{\mathrm{A}} = \left[\mathbf{e}_{R^k_{\mathrm{A}}(1)} \ \mathbf{e}_{R^k_{\mathrm{A}}(2)} \ \cdots \ \mathbf{e}_{R^k_{\mathrm{A}}(G)} \right]$, $\mathbf{e}_{R^k_{\mathrm{A}}(i)} = \left[\mathbf{0}_{R^k_{\mathrm{A}}(i)} \ 1 \ \mathbf{0}_{N-R^k_{\mathrm{A}}(i)} \right]$,

$$\mathbf{\Omega}^k_{\mathrm{B,m}} = (\mathbf{F}_{\mathrm{B}})^{\mathrm{T}} \mathbf{S}^k_{\mathrm{B,m}} \mathbf{E}_{\mathrm{B}}, \tag{15}$$

where $\mathbf{F}_{\mathrm{B}} = \left[\mathbf{f}_{D^k_{\mathrm{B}}(1)} \ \mathbf{f}_{D^k_{\mathrm{B}}(2)} \ \cdots \ \mathbf{f}_{D^k_{\mathrm{B}}(W)} \right]$, $\mathbf{f}_{D^k_{\mathrm{B}}(i)} = \left[\mathbf{0}_{D^k_{\mathrm{B}}(i)} \ 1 \ \mathbf{0}_{M-D^k_{\mathrm{B}}(i)} \right]$, $\mathbf{E}_{\mathrm{B}} = \left[\mathbf{e}_{R^k_{\mathrm{B}}(1)} \ \mathbf{e}_{R^k_{\mathrm{B}}(2)} \ \cdots \ \mathbf{e}_{R^k_{\mathrm{B}}(G)} \right]$, $\mathbf{e}_{R^k_{\mathrm{B}}(i)} = \left[\mathbf{0}_{R^k_{\mathrm{B}}(i)} \ 1 \ \mathbf{0}_{N-R^k_{\mathrm{B}}(i)} \right]$.

The data transmitted from local radars to the fusion center consist of two $W \times G$ matrices and a 8×1 vector containing the starting and ending indexes $\mathbf{\Psi}^k = (R^k_{\mathrm{A}}(1), R^k_{\mathrm{A}}(G), D^k_{\mathrm{A}}(1), D^k_{\mathrm{A}}(W), R^k_{\mathrm{B}}(1), R^k_{\mathrm{B}}(G), D^k_{\mathrm{B}}(1), D^k_{\mathrm{B}}(W))$ of the selected areas. The censored signals in range-Doppler domain are used for alignment to reduce the transmission from $2 \times N \times M$ to $(2 \times W \times G + 8)$ compared with the traditional echo transmission method, and $W << N, G << M$. In the fusion center, the signals from radars A and B in range-Doppler domain are reconstructed based on $\mathbf{\Omega}^k_{\mathrm{A}}$, $\mathbf{\Omega}^k_{\mathrm{B}}$ and the indexes $\mathbf{\Psi}^k$. The reconstructed signals from radars A and B in range-Doppler domain can be represented as

$$\mathbf{\Phi}^k_{\mathrm{A,m}} = \begin{bmatrix} \mathbf{0}_{\left(N-D^k_{\mathrm{A}}(W)\right)\times R^k_{\mathrm{A}}(1)} & \mathbf{0}_{\left(N-D^k_{\mathrm{A}}(W)\right)\times\left(R^k_{\mathrm{A}}(G)-R^k_{\mathrm{A}}(1)\right)} & \mathbf{0}_{\left(N-D^k_{\mathrm{A}}(W)\right)\times\left(M-R^k_{\mathrm{A}}(G)\right)} \\ \mathbf{0}_{\left(D^k_{\mathrm{A}}(W)-D^k_{\mathrm{A}}(1)\right)\times R^k_{\mathrm{A}}(1)} & \mathbf{\Omega}^k_{\mathrm{A,m}} & \mathbf{0}_{\left(D^k_{\mathrm{A}}(W)-D^k_{\mathrm{A}}(1)\right)\times\left(M-R^k_{\mathrm{A}}(G)\right)} \\ \mathbf{0}_{\left(D^k_{\mathrm{A}}(1)-1\right)\times R^k_{\mathrm{A}}(1)} & \mathbf{0}_{\left(D^k_{\mathrm{A}}(1)-1\right)\times\left(R^k_{\mathrm{A}}(G)-R^k_{\mathrm{A}}(1)\right)} & \mathbf{0}_{\left(D^k_{\mathrm{A}}(1)-1\right)\times\left(M-R^k_{\mathrm{A}}(G)\right)} \end{bmatrix}, \tag{16}$$

$$\boldsymbol{\Phi}_{\mathrm{B,m}}^{k}=\begin{bmatrix}\mathbf{0}_{\left(N-D_{\mathrm{B}}^{k}(W)\right)\times R_{\mathrm{B}}^{k}(1)} & \mathbf{0}_{\left(N-D_{\mathrm{B}}^{k}(W)\right)\times\left(R_{\mathrm{B}}^{k}(G)-R_{\mathrm{B}}^{k}(1)\right)} & \mathbf{0}_{\left(N-D_{\mathrm{B}}^{k}(W)\right)\times\left(M-R_{\mathrm{B}}^{k}(G)\right)}\\ \mathbf{0}_{\left(D_{\mathrm{B}}^{k}(W)-D_{\mathrm{B}}^{k}(1)\right)\times R_{\mathrm{B}}^{k}(1)} & \boldsymbol{\Omega}_{\mathrm{B,m}}^{k} & \mathbf{0}_{\left(D_{\mathrm{B}}^{k}(W)-D_{\mathrm{B}}^{k}(1)\right)\times\left(M-R_{\mathrm{B}}^{k}(G)\right)}\\ \mathbf{0}_{\left(D_{\mathrm{B}}^{k}(1)-1\right)\times R_{\mathrm{B}}^{k}(1)} & \mathbf{0}_{\left(D_{\mathrm{B}}^{k}(1)-1\right)\times\left(R_{\mathrm{B}}^{k}(G)-R_{\mathrm{B}}^{k}(1)\right)} & \mathbf{0}_{\left(D_{\mathrm{B}}^{k}(1)-1\right)\times\left(M-R_{\mathrm{B}}^{k}(G)\right)}\end{bmatrix}, \tag{17}$$

respectively. Then, we can align the data coming from radar B to radar A. Based on the alignment model in (13), the measurements from radar B after alignment can be expressed as

$$\boldsymbol{\Gamma}_{\mathrm{B,m}}^{k}=(\mathbf{V}_{\mathrm{B}})^{\mathrm{T}}\boldsymbol{\Phi}_{\mathrm{B,m}}^{k}\mathbf{U}_{\mathrm{B}}, \tag{18}$$

where $\mathbf{V}_{\mathrm{B}}=\left[\mathbf{v}_{X_{\mathrm{B}}^{k}(1)}\ \mathbf{v}_{X_{\mathrm{B}}^{k}(2)}\ \cdots\ \mathbf{v}_{X_{\mathrm{B}}^{k}(W)}\right]$, $\mathbf{v}_{X_{\mathrm{B}}^{k}(i)}=\left[\mathbf{0}_{X_{\mathrm{B}}^{k}(i)}\ 1\ \mathbf{0}_{M-X_{\mathrm{B}}^{k}(i)}\right]$, $\mathbf{U}_{\mathrm{B}}=\left[\mathbf{u}_{Y_{\mathrm{B}}^{k}(1)}\ \mathbf{u}_{Y_{\mathrm{B}}^{k}(2)}\ \cdots\ \mathbf{u}_{Y_{\mathrm{B}}^{k}(G)}\right]$, $\mathbf{u}_{Y_{\mathrm{B}}^{k}(i)}=\left[\mathbf{0}_{Y_{\mathrm{B}}^{k}(i)}\ 1\ \mathbf{0}_{N-Y_{\mathrm{B}}^{k}(i)}\right]$. It is worth mentioning that $Y_{\mathrm{B}}^{k}(i)$ is not always an integer, it can be interpolated from the adjacent point (integer time) locations: $l_{\mathrm{B}}^{k}(i)=\left\lfloor Y_{\mathrm{B}}^{k}(i)\right\rfloor$ and $h_{\mathrm{B}}^{k}(i)=\left\lceil Y_{\mathrm{B}}^{k}(i)\right\rceil$, where $\lfloor\ \rfloor$ and $\lceil\ \rceil$ are the round operators towards minus and plus infinity. After the interpolation in range-Doppler domain, (18) can be rewritten as

$$\boldsymbol{\Gamma}_{\mathrm{B,m}}^{k}=\left(\boldsymbol{\sigma}*(\mathbf{V}_{\mathrm{B}})^{\mathrm{T}}\boldsymbol{\Phi}_{\mathrm{B,m}}^{k}\mathbf{U}_{\mathrm{B}_{l}}+\boldsymbol{\omega}*(\mathbf{V}_{\mathrm{B}})^{\mathrm{T}}\boldsymbol{\Phi}_{\mathrm{B,m}}^{k}\mathbf{U}_{B_{h}}\right), \tag{19}$$

where $\mathbf{U}_{\mathrm{B}_{l}}=\left[\mathbf{u}_{l_{\mathrm{B}}^{k}(1)}\ \mathbf{u}_{l_{\mathrm{B}}^{k}(2)}\ \cdots\ \mathbf{u}_{l_{\mathrm{B}}^{k}(G)}\right]$, $\mathbf{U}_{B_{h}}=\left[\mathbf{u}_{h_{\mathrm{B}}^{k}(1)}\ \mathbf{u}_{h_{\mathrm{B}}^{k}(2)}\ \cdots\ \mathbf{u}_{h_{\mathrm{B}}^{k}(G)}\right]$,

$$\boldsymbol{\sigma}=\begin{bmatrix}1-\phi_1 & 1-\phi_1 & \cdots & 1-\phi_1 & \cdots & 1-\phi_1\\ 1-\phi_2 & 1-\phi_2 & \cdots & 1-\phi_2 & \cdots & 1-\phi_2\\ \vdots & \vdots & \ddots & \vdots & \ddots & \vdots\\ 1-\phi_i & 1-\phi_i & \cdots & 1-\phi_i & \cdots & 1-\phi_i\\ \vdots & \vdots & \ddots & \vdots & \ddots & \vdots\\ 1-\phi_W & 1-\phi_W & \cdots & 1-\phi_W & \cdots & 1-\phi_W\end{bmatrix}_{W\times G}, \tag{20}$$

$$\boldsymbol{\omega}=\begin{bmatrix}\phi_1 & \phi_1 & \cdots & \phi_1 & \cdots & \phi_1\\ \phi_2 & \phi_2 & \cdots & \phi_2 & \cdots & \phi_2\\ \vdots & \vdots & \ddots & \vdots & \ddots & \vdots\\ \phi_i & \phi_i & \cdots & \phi_i & \cdots & \phi_i\\ \vdots & \vdots & \ddots & \vdots & \ddots & \vdots\\ \phi_W & \phi_W & \cdots & \phi_W & \cdots & \phi_W\end{bmatrix}_{W\times G}, \tag{21}$$

and $\phi_i=Y_{\mathrm{B}}^{k}(i)-\left\lfloor Y_{\mathrm{B}}^{k}(i)\right\rfloor$. In (19), $*$ is Hadamard product, and its elements are defined as the product of the corresponding elements of two matrices.

When radars A and B detect the same targets, the ranges of the target to radars A and B are different, and the radar cross sections (RCS) at different angles are also different. Therefore, the amplitudes of the signals in range-Doppler domain from radars A and B are different, and the ratio of amplitudes is denoted as η. Therefore, the true values $\boldsymbol{\Omega}_{\mathrm{A,t}}^{k}$ and $\boldsymbol{\Gamma}_{\mathrm{B,t}}^{k}$ can be expressed as

$$\boldsymbol{\Omega}_{\mathrm{A,t}}^{k}=\eta\boldsymbol{\Gamma}_{\mathrm{B,t}}^{k}. \tag{22}$$

We get the following equations for the measurement models

$$\mathbf{\Omega}^k_{\mathrm{A,m}} = \mathbf{\Omega}^k_{\mathrm{A},t} + \boldsymbol{\varepsilon}^k_{\mathrm{A}}, \tag{23}$$

$$\mathbf{\Gamma}^k_{\mathrm{B,m}} = \mathbf{\Gamma}^k_{\mathrm{B},t} + \boldsymbol{\varepsilon}^k_{\mathrm{B}}, \tag{24}$$

where the random measurement noises $\boldsymbol{\varepsilon}_{\mathrm{A}}$, $\boldsymbol{\varepsilon}_{\mathrm{B}}$ are zero-mean Gaussian noises with covariance matrices $\mathbf{\Sigma}_{\mathrm{A}}$, $\mathbf{\Sigma}_{\mathrm{B}}$, respectively. By making use of (23) and (24), (22) can be rewritten as

$$\mathbf{\Omega}^k_{\mathrm{A,m}} = \eta \mathbf{\Gamma}^k_{\mathrm{B,m}} + \boldsymbol{\varepsilon}^k, \tag{25}$$

where $\boldsymbol{\varepsilon}$ is a zero-mean Gaussian random noise with covariance matrix $\mathbf{\Sigma} = \mathbf{\Sigma}_{\mathrm{A}} + \eta^2 \mathbf{\Sigma}_B$. Cross-correlation is the optimal approach to aligning the signals, in a minimum mean square error (MMSE) sense, when the signal noise is Gaussian. The parameter vector to be estimated is given by

$$\mathbf{\Theta} = \left(\alpha, \beta, \gamma, r_x, r_y, r_z\right)^{\mathrm{T}}. \tag{26}$$

To align signals coming from radar B to radar A, the alignment in range-Doppler domain can be formulated as the following optimization problem

$$J_1(\mathbf{\Theta}) = \sum_{k=1}^{K} \mathrm{corr}\left(\mathbf{\Omega}^k_{\mathrm{A,m}}, \mathbf{\Gamma}^k_{\mathrm{B,m}}\right), \tag{27}$$

where $\mathrm{corr}(\mathbf{X}, \mathbf{Y}) = \frac{(\mathrm{vec}(\mathbf{X}))^T(\mathrm{vec}(\mathbf{Y}))}{\sqrt{\left((\mathrm{vec}(\mathbf{X}))^T(\mathrm{vec}(\mathbf{X}))\right)\left((\mathrm{vec}(\mathbf{Y}))^T(\mathrm{vec}(\mathbf{Y}))\right)}}$, the vectorization operator $\mathrm{vec}(\cdot)$ stacks the columns vectors of the argument matrix into a long column vector in chronological order. The estimate $\mathbf{\Theta}$ can be obtained by maximizing the objective function $J_1(\mathbf{\Theta})$.

Symmetrically, to align the range-Doppler signal coming from radar A to radar B, the alignment can be formulated as the similar optimization problem

$$J_2(\mathbf{\Theta}) = \sum_{k=1}^{K} \mathrm{corr}\left(\mathbf{\Gamma}^k_{\mathrm{A,m}}, \mathbf{\Omega}^k_{\mathrm{B,m}}\right), \tag{28}$$

where

$$\mathbf{\Gamma}^k_{\mathrm{A,m}} = \boldsymbol{\sigma}' * (\mathbf{V}_{\mathrm{A}})^{\mathrm{T}} \mathbf{\Phi}^k_{\mathrm{A,m}} \mathbf{U}_{\mathrm{A}_l} + \boldsymbol{\omega}' * (\mathbf{V}_{\mathrm{A}})^{\mathrm{T}} \mathbf{\Phi}^k_{\mathrm{A,m}} \mathbf{U}_{\mathrm{A}_h}, \tag{29}$$

and $\mathbf{V}_{\mathrm{A}} = \left[\mathbf{v}_{X^k_{\mathrm{A}}(1)}\ \mathbf{v}_{X^k_{\mathrm{A}}(2)}\ \cdots\ \mathbf{v}_{X^k_{\mathrm{A}}(W)}\right]$, $\mathbf{U}_{\mathrm{A}_l} = \left[\mathbf{u}_{l^k_{\mathrm{A}}(1)}\ \mathbf{u}_{l^k_{\mathrm{A}}(2)}\ \cdots\ \mathbf{u}_{l^k_{\mathrm{A}}(G)}\right]$, $\mathbf{U}_{\mathrm{A}_h} = \left[\mathbf{u}_{h^k_{\mathrm{A}}(1)}\ \mathbf{u}_{h^k_{\mathrm{A}}(2)}\ \cdots\ \mathbf{u}_{h^k_{\mathrm{A}}(G)}\right]$. The definitions of $\mathbf{v}_{X^k_{\mathrm{A}}(i)}$, $\mathbf{u}_{l^k_{\mathrm{A}}(i)}$, $\mathbf{u}_{h^k_{\mathrm{A}}(i)}$, $\boldsymbol{\sigma}'$ and $\boldsymbol{\omega}'$ are similar to those of $\mathbf{v}_{X^k_{\mathrm{B}}(i)}$, $\mathbf{u}_{l^k_{\mathrm{B}}(i)}$, $\mathbf{u}_{h^k_{\mathrm{B}}(i)}$, $\boldsymbol{\sigma}$ and $\boldsymbol{\omega}$, and they will not be repeated here.

Therefore, the optimization problem for alignment can be rewritten as

$$J(\mathbf{\Theta}) = J_1(\mathbf{\Theta}) + J_2(\mathbf{\Theta}). \tag{30}$$

The estimate $\mathbf{\Theta}$ can be obtained by maximizing the objective function $J(\mathbf{\Theta})$.

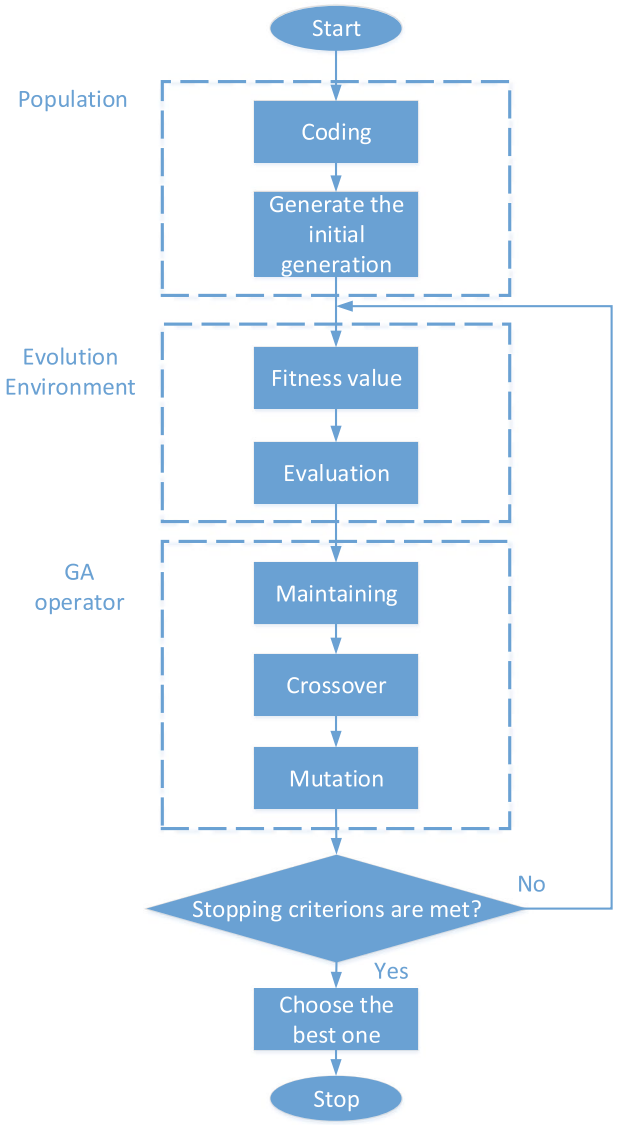

Fig. 7 The flow diagram for genetic algorithm

3.3 Genetic algorithm

To solve the estimate $\boldsymbol{\Theta}$ in (30), a genetic algorithm (GA) is used to maximize $J(\boldsymbol{\Theta})$ in this subsection. GAs [28] are one of the most widely used artificial intelligent techniques for optimization. A GA is a stochastic searching algorithm based on the mechanisms of natural selection and genetics. GAs have been proven to be very efficient and stable in searching for global optimum solutions. Usually, a GA is mainly composed of three operations: initial population, evolution environment, genetic operation (see Fig. 7). A brief summary for a GA can be summarized as follows.

(1) Initial population:

The GA starts the iteration with the initial population as the initial values. The initial population size n_p represents the number of individuals in the population. The initial set of population $\mathbf{\Theta}^{\mathrm{I}}$ is usually generated by coding as follow

$$\begin{array}{l} \mathbf{\Theta}^{\mathrm{I}} = \left\{\mathbf{\Theta}_1, \mathbf{\Theta}_2, \cdots, \mathbf{\Theta}_{n_p}\right\} \\ \mathbf{\Theta}_i = \left[\mathbf{\Theta}_{i,1}, \mathbf{\Theta}_{i,2}, \cdots, \mathbf{\Theta}_{i,j}, \cdots, \mathbf{\Theta}_{i,n_v}\right] \\ i = 1, 2, \cdots, n_p \\ j = 1, 2, \cdots, n_v \\ \mathbf{\Theta}_j^{\min} \le \mathbf{\Theta}_{i,j} \le \mathbf{\Theta}_j^{\max} \end{array}, \tag{31}$$

where n_v denotes the number of the estimated parameters, $\mathbf{\Theta}_j^{\min}$ and $\mathbf{\Theta}_j^{\max}$ are the minimum and maximum values of the parameter $\mathbf{\Theta}_{i,j}$. The initial population is usually generated randomly, but if the actual distribution of the population is known, the initial population can also be generated according to this distribution.

(2) Fitness Function:

The fitness function of the parameter vector $\mathbf{\Theta}$ is expressed as

$$fitness = J(\mathbf{\Theta}_i) \tag{32}$$

The form of the fitness function depends on the objective function in (30) of the algorithm.

(3) Genetic Operation:

The most important operations of a GA for solving objective functions are maintaining, reproduction, crossover, and mutation. A brief description of these operations is shown below [29].

(a) Maintaining: The individual with the highest fitness in this generation is copied to the next generation. It ensures that the best genes will not be destroyed in the next generation.

(b) Reproduction: Based on their fitness values, some individuals are selected to reproduce the next generation with the corresponding probability. The probability of the ith individual (corresponding to the ith chromosome $\mathbf{\Theta}_i$) with fitness value reproduced for crossover in the next generation is

$$P_i = \frac{J(\mathbf{\Theta}_i)}{\sum_{i'=1}^{n_p} J(\mathbf{\Theta}_{i'})}. \tag{33}$$

(c) Crossover: The crossover operation is mainly for exchanging information from the two parents, chromosomes $\mathbf{\Theta}_i$ and $\mathbf{\Theta}_{i+1}$. It is an effective method to create new combinations of genes.

(d) Mutation: Mutation is to create new individuals by changing the genes of the chromosomes with a small probability. The mutation operation ensures that the algorithm can search each value in the solution space to reach the global optimum.

The flowchart of the GA is summarized in Fig. 7. The GA is used to calculate the maximum value of the objective function in (30), and the optimal alignment parameter $\mathbf{\Theta}$ can be obtained. The pseudocode of the GA-based spatial alignment algorithm for networked radars in range-Doppler domain is shown in Algorithm 1.

Algorithm 1 Range-Doppler domain spatial alignment algorithm for networked radars

Require:
Signals from radars A and B in range-Doppler domain : $\mathbf{S}_{\mathrm{A,m}}^{k}$, $\mathbf{S}_{\mathrm{B,m}}^{k}$
Ensure:
$\boldsymbol{\Theta}$ as in (26)
for $k = 1:1:K$ **do**
Signals $\mathbf{S}_{\mathrm{A,m}}^{k}$ and $\mathbf{S}_{\mathrm{B,m}}^{k}$ from local radars in range-Doppler domain are obtained after preprocessing and signal processing.
The initial CFAR is used to select the informative data sets $\boldsymbol{\Omega}_{\mathrm{A,m}}^{k}$ and $\boldsymbol{\Omega}_{\mathrm{B,m}}^{k}$ in range-Doppler domain, as in (14) and (15).
The censored data sets $\boldsymbol{\Omega}_{\mathrm{A,m}}^{k}$ and $\boldsymbol{\Omega}_{\mathrm{B,m}}^{k}$ and the indexes of initial CFAR $\boldsymbol{\Psi}^{k}$ are transmitted from the local radars A and B to the fusion center.
Based on $\boldsymbol{\Omega}_{\mathrm{A,m}}^{k}$, $\boldsymbol{\Omega}_{\mathrm{B,m}}^{k}$ and $\boldsymbol{\Psi}^{k}$, $\boldsymbol{\Phi}_{\mathrm{A,m}}^{k}$ and $\boldsymbol{\Phi}_{\mathrm{B,m}}^{k}$ are reconstructed in the fusion center, as in (16) and (17).
The alignment model is established in (13) to estimate the alignment parameter $\boldsymbol{\Theta}$.
When radar A serves as the reference radar, $\boldsymbol{\Gamma}_{\mathrm{B,m}}^{k}$ from the registered radar B is obtained as in (19). Similarly, when radar B serves as the reference radar, $\boldsymbol{\Gamma}_{\mathrm{A,m}}^{k}$ can be obtained as in (29).
end for
The correlation function $J(\boldsymbol{\Theta}) = \sum_{k=1}^{K}\left(corr\left(\boldsymbol{\Omega}_{\mathrm{A,m}}^{k}, \boldsymbol{\Gamma}_{\mathrm{B,m}}^{k}\right) + corr\left(\boldsymbol{\Gamma}_{\mathrm{A,m}}^{k}, \boldsymbol{\Omega}_{\mathrm{B,m}}^{k}\right)\right)$ is established as the objective function.
A GA is used to solve the maximization problem $J(\boldsymbol{\Theta})$ to obtain the optimal alignment parameter $\boldsymbol{\Theta}$.
return Parameter vector $\boldsymbol{\Theta}$

It is worth mentioning that pairwise alignment is used when there are more than two radars in the multi-static radar systems. Without loss of generality, three radars are taken as an example. When the number of radars increases, the alignment method is similar to that in the situation of three radars. The radar A, B and C detect the targets independently. The alignment parameter vector between radars A and B, B and C, A and C can be expressed as $\boldsymbol{\Theta}_{\mathrm{AB}}$, $\boldsymbol{\Theta}_{\mathrm{BC}}$, $\boldsymbol{\Theta}_{\mathrm{AC}}$, respectively. The optimization problem $J(\boldsymbol{\Theta}_{\mathrm{AB}}, \boldsymbol{\Theta}_{\mathrm{BC}}, \boldsymbol{\Theta}_{\mathrm{AC}})$ can be solved by using the proposed algorithm.

4 Results and discussion

In this section, we present numerical examples to demonstrate the performance of the proposed algorithm. The coordinates of radars A and B are [1000; 300; 1000] m and [100; 10; 800] m, respectively, in local Cartesian coordinates (X-East, Y-North, Z-Up). Radars A and B detect targets using LFM signals, and the radar parameters are given in Table 1.

Radars A and B observe the target in their spatial coordinates with K CPIs. In our simulations, $K = 50$. The spatial alignment algorithm is simulated in single target and

Table 1 The radar parameters

Parameters	Radar A	Radar B
Carrier frequency f_c/GHz	10	9
Pulse width T_p/us	0.6	0.6
Pulse repetition period T_r/us	19	19
PRI number in one CPI N	256	256
Sampling rate f_s/MHz	50	50
Bandwidth B/MHz	5	4
Noise factor F_n/dB	5	6

multi-target scenarios, respectively. The value ranges for the initial populations of the parameters in $\boldsymbol{\Theta}$ are $\alpha \in [0, 2\pi)$rad, $\beta \in [0, 2\pi)$rad, $\gamma \in [0, 2\pi)$rad, $r_x \in [-1000, 1000]$m, $r_y \in [-1000, 1000]$m, $r_z \in [-1000, 1000]$m.

4.1 Single target scenario

The single target located at coordinates moves with a nearly constant acceleration (NCA) vector $(\ddot{x}, \ddot{y}, \ddot{z})$. A target state vector for NCA models [30, 31] is $\mathbf{s}^t = \left[x^t \ \dot{x}^t \ \ddot{x}^t \ y^t \ \dot{y}^t \ \ddot{y}^t \ z^t \ \dot{z}^t \ \ddot{z}^t \right]^{\mathrm{T}}$, where x^t, y^t, z^t are the position values of the target in X, Y, Z axes, $\dot{x}^t, \dot{y}^t, \dot{z}^t$ are the velocity values, $\ddot{x}^t, \ddot{y}^t, \ddot{z}^t$ are the acceleration values. The target state equation is given by

$$\mathbf{s}_{k+1}^t = \mathbf{F}_k \mathbf{s}_k^t + \mathbf{v}_k, \tag{34}$$

where

$$\mathbf{F}_k = \begin{bmatrix} \boldsymbol{\Psi}_k & \mathbf{0} & \mathbf{0} \\ \mathbf{0} & \boldsymbol{\Psi}_k & \mathbf{0} \\ \mathbf{0} & \mathbf{0} & \boldsymbol{\Psi}_k \end{bmatrix} \tag{35}$$

with $\boldsymbol{\Psi}_k$ being the transition matrix of the NCA model in a single dimension, and $\mathbf{0}$ being the zero matrix of dimension 3×3 for NCA target model. We have

$$\boldsymbol{\Psi}_k = \begin{bmatrix} 1 & T_k & T_k^2/2 \\ 0 & 1 & T_k \\ 0 & 0 & 1 \end{bmatrix}. \tag{36}$$

Index k corresponds to the time instant t_k and the sample interval is defined by $T_k = t_{k+1} - t_k$. Process noise $\mathbf{v}_k$ is white Gaussian with non-singular covariance matrix

$$\mathbf{Q}_k = \begin{bmatrix} \boldsymbol{\Lambda}_k & \mathbf{0} & \mathbf{0} \\ \mathbf{0} & \boldsymbol{\Lambda}_k & \mathbf{0} \\ \mathbf{0} & \mathbf{0} & \boldsymbol{\Lambda}_k \end{bmatrix}, \tag{37}$$

where

$$\boldsymbol{\Lambda}_k = q \begin{bmatrix} \frac{T_k^5}{20} & \frac{T_k^4}{8} & \frac{T_k^3}{6} \\ \frac{T_k^4}{8} & \frac{T_k^3}{3} & \frac{T_k^2}{2} \\ \frac{T_k^3}{6} & \frac{T_k^2}{2} & T_k \end{bmatrix}, \tag{38}$$

and q is the level of power spectral density of the corresponding continuous process noise.

The initial target state vector is

$$\mathbf{s}_0^t = \left[2500\text{m} \ 500\text{m/s} \ 10\text{m/s}^2 \ 90\text{m} \ 500\text{m/s} \ 60\text{m/s}^2 \ 1050\text{m} \ 500\text{m/s} \ 60\text{m/s}^2 \right]^{\mathrm{T}}. \tag{39}$$

The level of power spectral density of the corresponding continuous process noise is $q = 2$.

A GA is used to estimate the spatial alignment parameter $\boldsymbol{\Theta}$ in (30). Figure 8 shows the fitness function values for a single target. The generation for the X-axis in Fig. 8

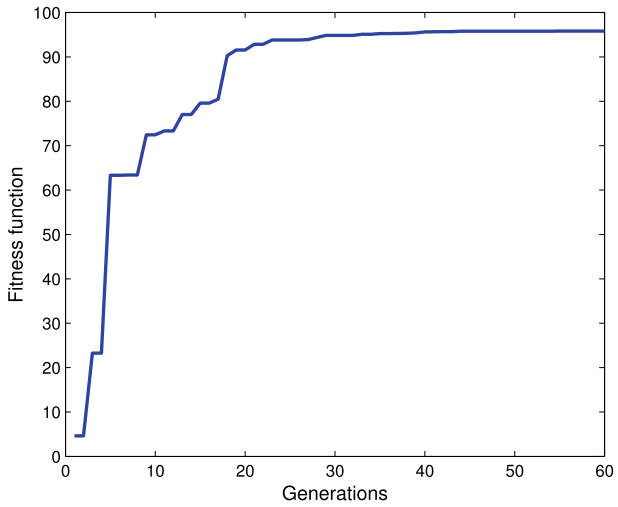

Fig. 8 The fitness function with generations for a single target

represents the index of new populations evolved from the initial population. The x generation population is obtained from the $x-1$ generation population after maintaining, crossover, and mutation. The stopping criterion of the GA is usually the number of generations. When the number of generations reaches 60, the iteration is stopped. As we can see, with the increase of generations, the value of fitness function increases, and the fitness function tends to be stable when it reaches the maximum value. Figure 9a–f show the estimated values and true values of $\alpha, \beta, \gamma, r_x, r_y, r_z$ in $\boldsymbol{\Theta}$, respectively. As generations grow, the estimated values gradually converge to the true values.

Radars A and B measure the target trajectory in their respective space coordinate systems. Therefore, there is considerable difference between the target trajectories from radars A and B before spatial alignment, as shown in Fig. 10a. Data fusion cannot be completed if the space is not aligned. In the absence of positions, attitudes of radars A and B, the spatial alignment vector $\boldsymbol{\Theta}$ can be estimated by using the proposed algorithm. The target trajectory from radar B after spatial alignment is shown in Fig. 10b compared with the trajectory from radar A. From Fig. 10b, the registered target trajectory from radar B approaches to the trajectory from radar A. The trajectories after alignment are in the same spatial coordinate system, which is an important prerequisite for successful fusion of networked radars.

4.2 Multiple-target scenario

For a multi-target scenario, it is assumed that data association problem has been solved by K-nearest neighbor algorithm [32]. Z maneuverable targets ($Z = 3$ in the simulations) independently fly along respective paths. The motion models of multiple targets are the same as that of the single target, i.e., NCA models. The initial values of state vectors for the three targets are given by

$$\mathbf{s}_0^{t_1} = \left[\, 2500\text{m}\ \ 500\text{m/s}\ \ 10\text{m/s}^2\ \ 90\text{m}\ \ 500\text{m/s}\ \ 60\text{m/s}^2\ \ 1050\text{m}\ \ 500\text{m/s}\ \ 60\text{m/s}^2 \,\right]^{\mathrm{T}}, \tag{40}$$

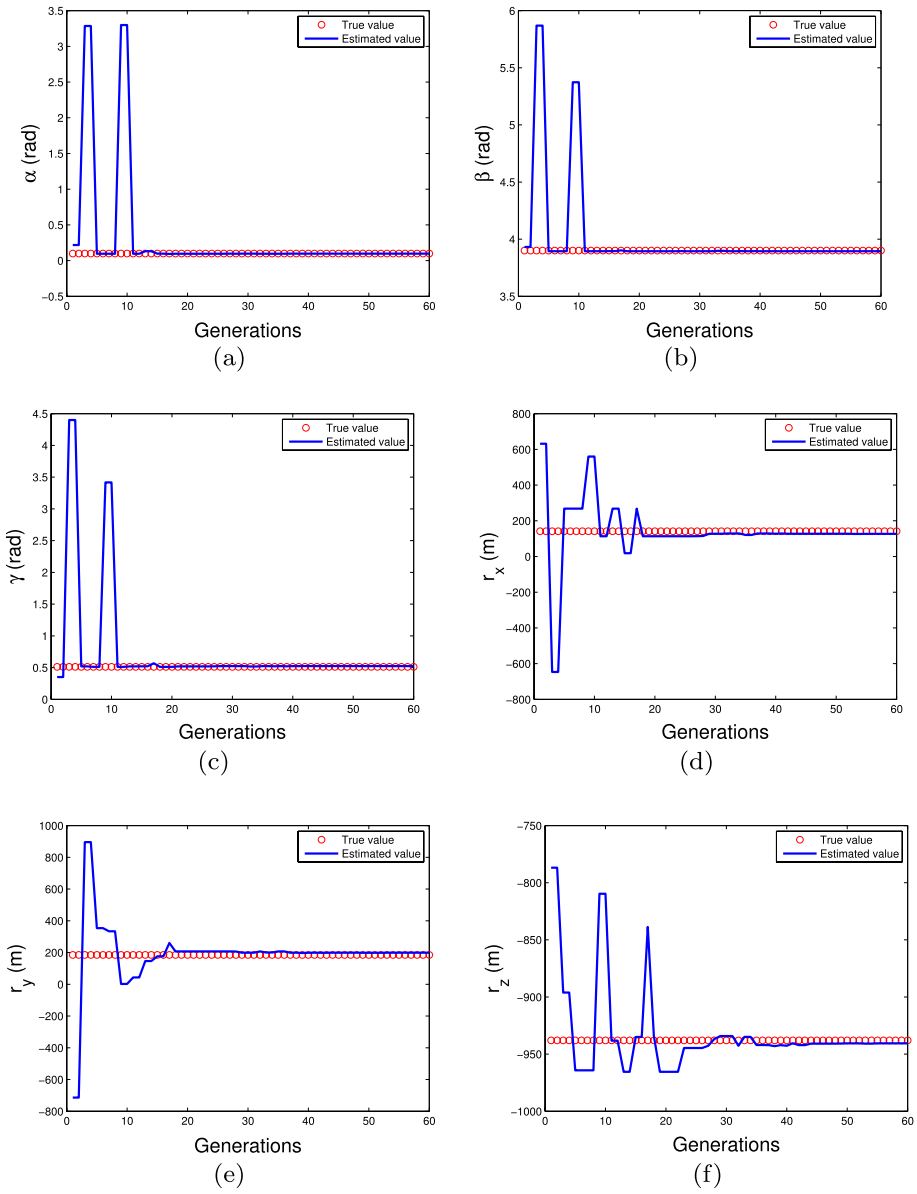

Fig. 9 Estimated values and true values with increase of generations for a single target

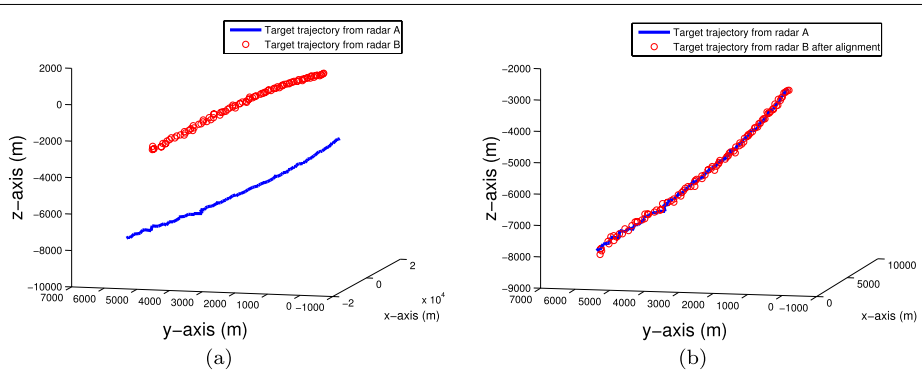

Fig. 10 Target trajectories from radars A and B **a** before alignment **b** after alignment

$$\mathbf{s}_0^{t_2} = \left[\, 4000\text{m}\ \ 650\text{m/s}\ \ 10\text{m/s}^2\ \ 100\text{m}\ \ 400\text{m/s}\ \ 120\text{m/s}^2\ \ 800\text{m}\ \ 800\text{m/s}\ \ 100\text{m/s}^2 \,\right]^{\mathrm{T}}, \tag{41}$$

$$\mathbf{s}_0^{t_3} = \left[\, 1000\text{m}\ \ 350\text{m/s}\ \ 10\text{m/s}^2\ \ 200\text{m}\ \ 400\text{m/s}\ \ 70\text{m/s}^2\ \ 1000\text{m}\ \ 600\text{m/s}\ \ 70\text{m/s}^2 \,\right]^{\mathrm{T}}. \tag{42}$$

Figure 11 shows fitness function values for multiple targets. As we can see, with the increase of generations, the value of fitness function increases, and the fitness function tends to be stable when it reaches the maximum value. Figure 12a–f show the estimated values and true values for $\alpha, \beta, \gamma, r_x, r_y, r_z$ in $\boldsymbol{\Theta}$, respectively. As generations grow, the estimated values gradually converge to the true values.

In Fig. 13a, radars A and B observe multi-target trajectories in their respective coordinate systems. The unregistered multi-target trajectories of radar B are deviated from the trajectories of radar A. Unregistered multi-target trajectories cannot be used for subsequent information fusion. In the proposed algorithm, spatial alignment vector $\boldsymbol{\Theta}$ is estimated in range-Doppler domain without the prior information (positions and attitudes) of radars. The multi-target trajectories from radar B after spatial alignment are shown in Fig. 13b compared with those from radar A. In Fig. 13b, the registered multi-target trajectories of radar B appear almost indistinguishable from those of radar A, indicating that the trajectories after alignment are in the same spatial coordinate system, and can be effectively used for information fusion.

4.3 Performance evaluation

In this subsection, the performance of the proposed algorithm is showed and compared with other methods. The data after alignment are fused by SNR weighting based method. The number of Monte Carlo trials is 500. Figure 14 shows the detection probabilities of the proposed algorithm and the monostatic radar (radar A) with different false alarm rate (P_f). The SNR for Fig. 14 and Fig. 15 is the SNR of the signal before CFAR detection, i.e., the SNR in range-Doppler domain, which is defined as the signal-to-noise power

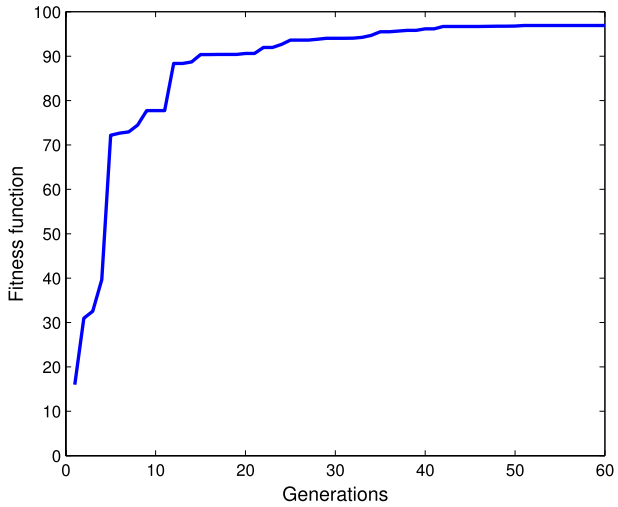

Fig. 11 The fitness function with generations for multiple targets

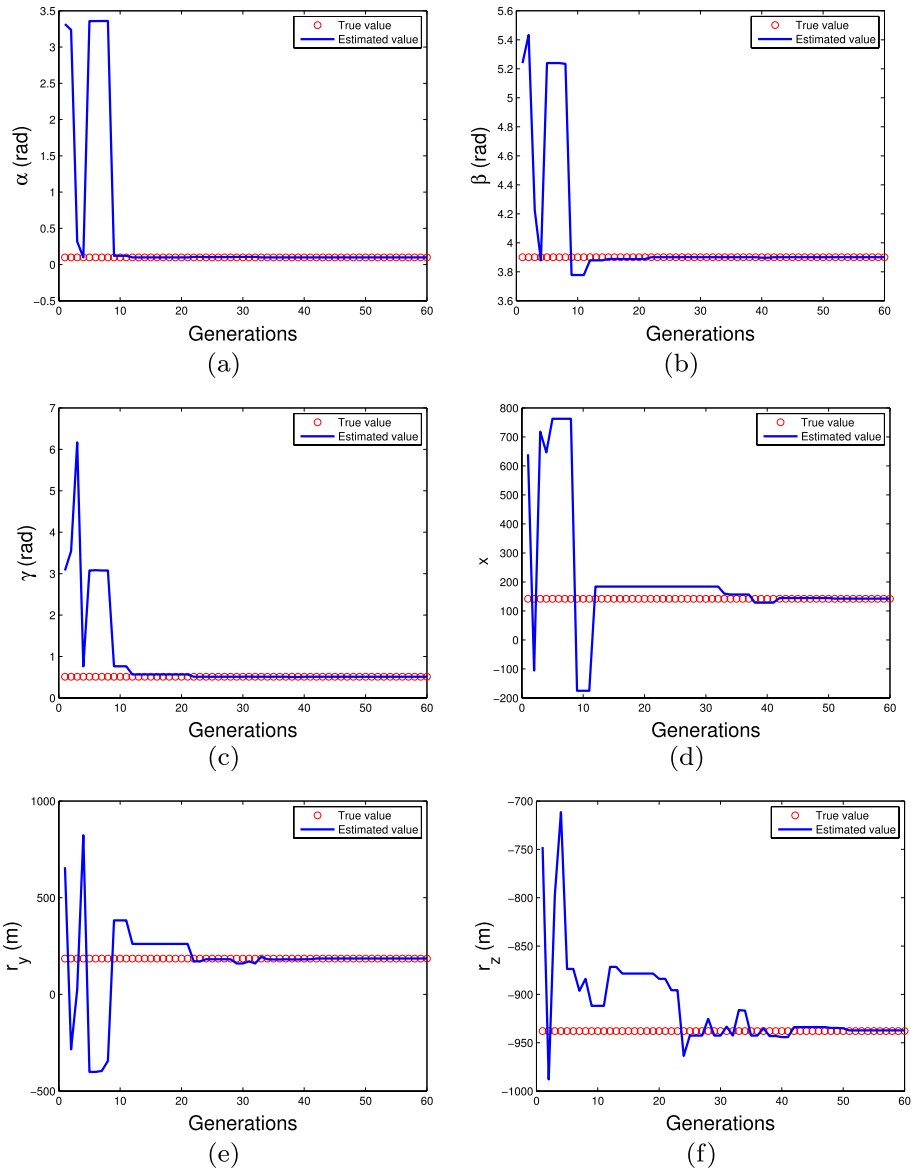

Fig. 12 Estimated values and true values with increase of generations for multitarget

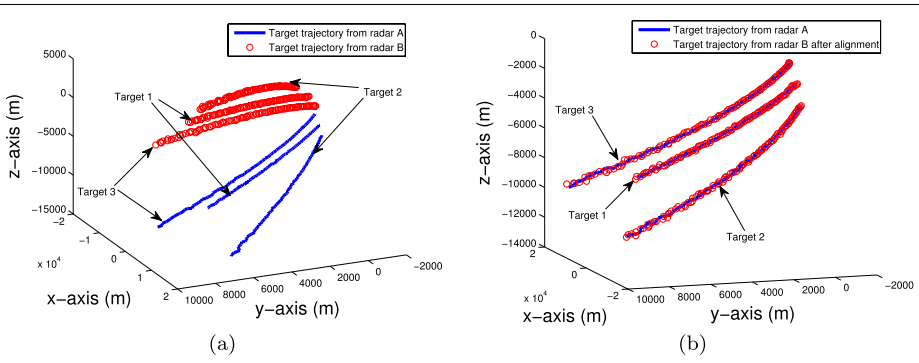

Fig. 13 Multi-target trajectories from radars A and B **a** before alignment **b** after alignment

Table 2 The SNRs required for the same detection probability (90%)

False alarm rate	10^{-4}	10^{-6}	10^{-8}
Monostatic radar	12.4 dB	14.2 dB	15.8 dB
Proposed alignment algorithm (two radar)	11.1 dB	13 dB	14.7 dB
Proposed alignment algorithm (three radar)	10.5 dB	12.6 dB	14.2 dB

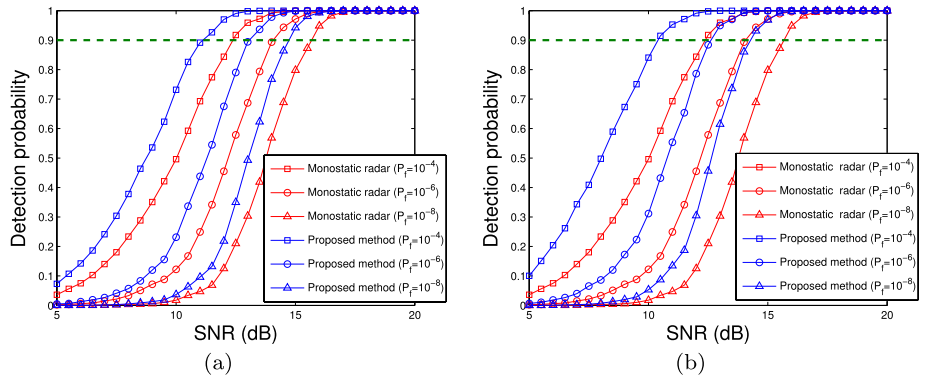

Fig. 14 The detection probability after alignment in different false alarm rate (P_f) **a** proposed method by two radars compared with the monostatic radar **b** proposed method by three radars compared with the monostatic radar

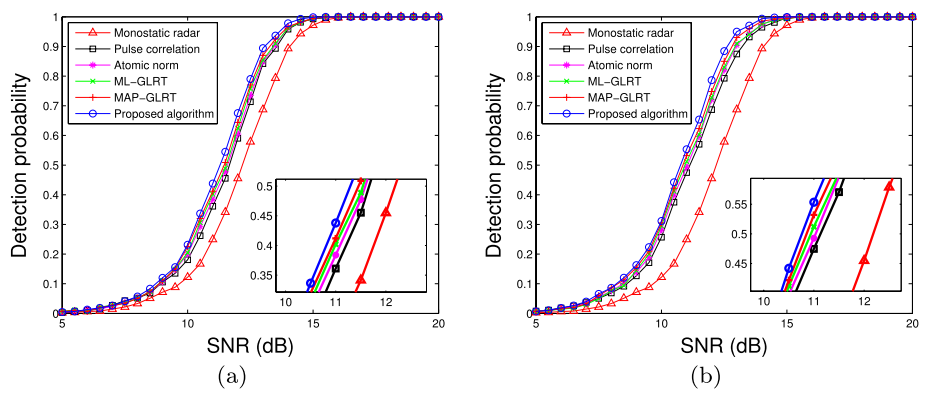

Fig. 15 The detection probability of the proposed algorithm compared with the monostatic radar, pulse correlation method, atomic norm optimization, ML-GLRT and MAP-GLRT **a** alignment by two radars **b** alignment by three radars

ratio for the signal in range-Doppler domain before CFAR detection. For example, it is assumed that the SNR of the echo signal is S_0, the bandwidth of the LFM signal is B, the pulse width is T_p, the point number of FFT in MTD is N_F. The SNR in range-Doppler domain can be expressed as

$$\mathrm{SNR} = BT_pN_FS_0. \tag{43}$$

For the same detection probability (90%), the SNRs required by the proposed fusion algorithm are shown in Table 2 compared with those by the monostatic radar. The improvements of SNR after alignment using the proposed algorithm for two and three radars are 1.1 dB and 1.6 dB, respectively. But apparently, with the increase of the number of radars, the number of parameters to be estimated also increases in direct proportion. Therefore, the calculation of the alignment algorithm increases.

Figure 15a, b shows the detection probability by two radars and three radars after alignment respectively, and the detection probability of the proposed algorithm is compared with the monostatic radar, pulse correlation method [18], atomic norm optimization method [23], ML-GLRT and MAP-GLRT [20]. The false alarm rate is 10^{-6}. From Fig. 15, the detection probability increases with the increase of SNR. It shows that the detection probability for networked radars is improved compared with that from the monostatic radar at the same SNR. When the number of radars in the cooperative detection system increases, the detection probability increases after alignment and fusion, shown in comparison between Fig. 15a, b. Moreover, the detection probability of the proposed algorithm is improved compared with pulse correlation method [18], atomic norm optimization method [23], ML-GLRT and MAP-GLRT [20] at the same SNR.

In order to verify the tracking accuracy after alignment and fusion using the proposed algorithm, Fig. 16a–c show the root-mean-square error (RMSE) of the target state estimation achieved by the proposed algorithm in X, Y, Z axes, respectively, compared with

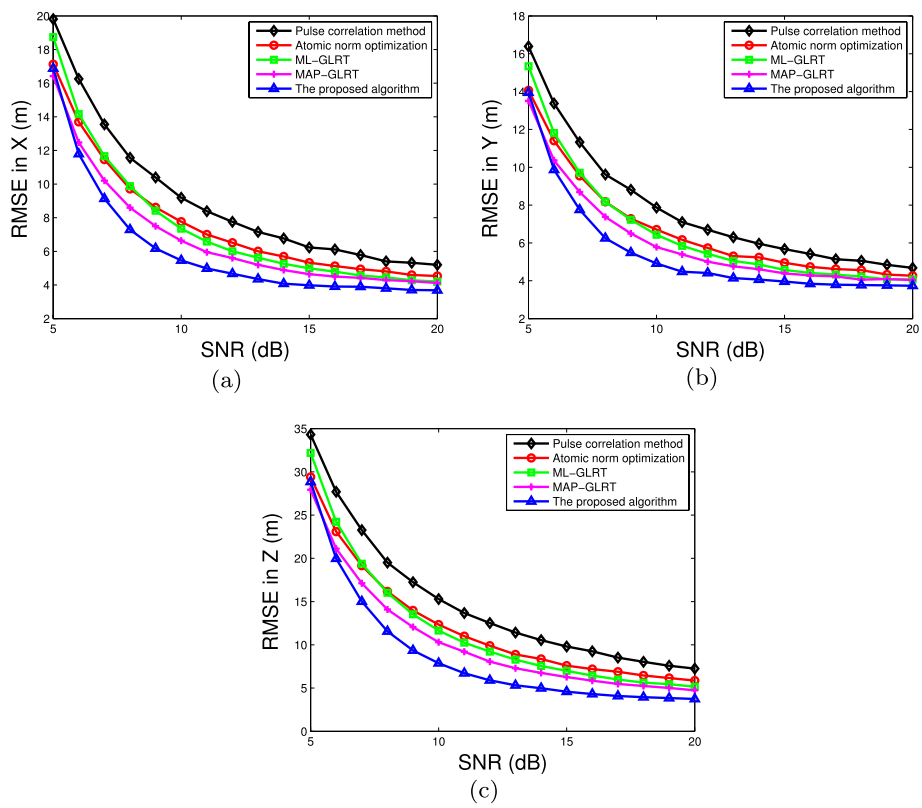

Fig. 16 RMSE of the proposed alignment algorithm compared with the other methods **a** in X axis **b** in Y axis **c** in Z axis

the pulse correlation method [18], atomic norm optimization method [23], ML-GLRT and MAP-GLRT [20]. For a scalar ξ , the RMSE from N Monte Carlo runs with estimated error $\tilde{\xi}_i$ in run i is defined as [31]

$$\mathrm{RMSE}(\tilde{\xi}) = \sqrt{\frac{1}{N}\sum_{i=1}^{N}\tilde{\xi}_i^2}, \tag{44}$$

where $\tilde{\xi}_i = \xi_i - \hat{\xi}_i$. The value $\hat{\xi}_i$ is the estimated value of ξ. In this subsection, ξ is the target position in X, Y, Z axes. It can be seen that the performance of tracking using the proposed algorithm is better.

5 Conclusions

In this paper, a low-communication-rate spatial alignment in range-Doppler domain was proposed for networked radars without the prior information (positions and attitudes) of radars. The signal in range-Doppler domain was censored to select the informative data for alignment by initial CFAR detection, which greatly reduced the communication-rate between local radars and the fusion center. Based on the alignment model in geometry, the alignment optimization problem was established in range-Doppler domain. Spatial registration parameters were estimated by a GA. The signals after alignment were in the same spatial coordinate system, and can be effectively used for information fusion. The detection probability and the tracking accuracy of the proposed algorithm at the same SNR were improved after alignment and fusion compared with state-of-art methods.

Abbreviations

SNR: Signal-to-noise rate; CFAR: Constant false alarm rate; CPI: Coherent processing interval; PRI: Pulse repetition interval; GA: Genetic algorithm; KF: Kalman filter; EKF: Extended Kalman filter; UKF: Unscented Kalman filter; LS: Least square; ELS: Exact least square; MLR: Maximum likelihood registration; PHD: Probability hypothesis density; 3D: Three-dimensional; MTD: Moving target detection; LFM: Linear frequency modulation; DBF: Digital beam forming; FFT: Fast Fourier transform; RCS: Radar cross sections; NCA: Nearly constant acceleration; RMSE: Root-mean-square error.

Acknowledgements

The authors would like to acknowledge all the participants for their contributions to this research.

Authors' information

Xiaoyu Cong was born in 1991. She received the M.S. degree from the School of Information and Control Engineering, China University of Mining and Technology. She is currently pursuing the Ph.D. degree with the Department of Communication and Information System, Nanjing University of Science and Technology. Her current research interests include radar signal processing, information alignment, and data fusion.

Yubing Han was born in 1971. He received the Ph.D. degree in signal and information processing from Southeast University, China, in 2006. Since 2006, he has been a Faculty Member with the School of Electronic and Optical Engineering, NJUST, where he is currently a Professor. His current research interests include array signal processing, radar signal processing, wireless communications, and digital image processing.

Weixing Sheng was born in 1966. He received his M.S. degree in Department of Communication and Information System in 1991 and received his Ph.D. degree in Department of Electromagnetic Field and Electromagnetic Waves in 2002 from Nanjing University of Science and Technology. His current research interests include radar signal processing, modeling and application of electromagnetic scattering.

Shanhong Guo was born in 1969. She received the Ph.D. degree from Department of Communication and Information System, Nanjing University of science and technology. Her current research interests include radar signal processing, communication and information system.

Hui Sun received the Ph.D. degree in electrical engineering from Louisiana State University, Baton Rouge, LA, USA, in 2016. He is currently working in School of Electronic and Optical Engineering, Nanjing University of Science and Technology, Nanjing, China. His current research interests include cooperative relay networks and cognitive radio networks.

Author contributions

X.Y.C. proposed the range-Doppler domain spatial alignment and carried out the simulation experiments. Y.B.H. proposed the paper organization. W.X.S. analyzed the alignment model and performance. S.H.G. analyzed the data. H.S. improved the writing. All authors read and approved the final manuscript.

Funding
This work is supported in part by the National Natural Science Foundation of China (Grant No. 11273017).

Availability of data and materials
The datasets used during the current study are available from the corresponding author on reasonable request.

Declarations

Competing interests
The authors declare that they have no competing interests.

Received: 9 August 2021 Accepted: 8 February 2022
Published online: 20 February 2022

References

1. X. Song, N. Zheng, S. Yan, H. Li, A joint resource allocation method for multiple targets tracking in distributed mimo radar systems. EURASIP J. Adv. Signal Process. **1**, 2018 (2018)
2. D. Cormack, I. Schlangen, J.R. Hopgood, D.E. Clark, Joint registration and fusion of an infrared camera and scanning radar in a maritime context. IEEE Trans. Aerosp. Electron. Syst. **56**(2), 1357–1369 (2020)
3. Y.F. Shi, S.H. Park, T.L. Song, Multitarget tracking in cluttered environment for a multistatic passive radar system under the DAB/DVB network. Eur. J. Adv. Signal Process. **2017**(1), 11 (2017)
4. L. Ding, C. Shi, W. Qiu, J. Zhou, Joint dwell time and bandwidth optimization for multi-target tracking in radar network based on low probability of intercept. Sensors **20**(5), 1269 (2020)
5. D. Cormack, J.R. Hopgood, Message passing and hierarchical models for simultaneous tracking and registration. IEEE Trans. Aerosp. Electron. Syst. **57**(3), 1524–1537 (2021)
6. W. Wu, J. Jing, W. Liu, X. Feng, L. GAO, X. Qin, Augmented state GM-PHD filter with registration errors for multi-target tracking by doppler radars. Signal Process. **120**(C), 117–128 (2016)
7. E. Taghavi, R. Tharmarasa, T. Kirubarajan, Y. Bar-Shalom, M. Mcdonald, A practical bias estimation algorithm for multisensor-multitarget tracking. IEEE Trans. Aerosp. Electron. Syst. **52**(1), 2–19 (2016)
8. A. Burguera, F. Bonin-Font, G. Oliver, Towards robust image registration for underwater visual SLAM, in *International Conference on Computer Vision Theory and Applications*. IEEE (2015)
9. C. Guo, X. Tong, S. Liu, X. Lu, H. Xie, High-precision attitude estimation method of star sensors and gyro based on complementary filter and unscented Kalman filter. ISPRS Int. Arch. Photogramm. Remote Sens. Spatial Inf. Sci. **XLII–3/W1**, 49–53 (2017)
10. H. Chen, X. Cheng, C. Dai, F. Liu, Robust stability analysis of H-SGQKF and its application to transfer alignment. Signal Process. **117**, 310–321 (2015)
11. S. Fortunati, A. Farina, F. Gini, A. Graziano, M.S. Greco, S. Giompapa, Least squares estimation and Cramér-Rao type lower bounds for relative sensor registration process. IEEE Trans. Signal Process. **59**(3), 1075–1087 (2011)
12. D. Li, D. Wu, P. Lou, Exact least square registration algorithm for multiple dissimilar sensors, in *2017 10th International Symposium on Computational Intelligence and Design (ISCID)* (2017)
13. B. Ristic, N. Okello, Maximum likelihood registration for multiple dissimilar sensors. IEEE Trans. Aerosp. Electron. Syst. **29**(3), 1074–1083 (2003)
14. L. Chai, W. Yi, X. Jiang, L. Kong, A distributed phd filter for on-line joint sensor registration and multi-target tracking, in *22nd International Conference on Information Fusion* (2019)
15. X. Cong, Y. Han, W. Sheng, S. Guo, R. Zhang, Spatio-temporal alignment and trajectory matching for netted radar without prior spatial information and time delay. IEEE Access **PP**(99), 1–1 (2020)
16. A. Kurobe, Y. Sekikawa, K. Ishikawa, H. Saito, Corsnet: 3d point cloud registration by deep neural network. IEEE Robot. Autom. Lett. **5**(3), 3960–3966 (2020)
17. W. Ma, J. Zhang, Y. Wu, L. Jiao, H. Zhu, W. Zhao, A novel two-step registration method for remote sensing images based on deep and local features. *IEEE Trans. Geosci. Remote Sens.*, 1–10 (2019)
18. N. O'Donoughue, J.M.F. Moura, Y. Jin, Signal-domain registration for change detection in time-reversal sar, in *Conference on Signals, Systems and Computers* (2008)
19. S. Wei, L. Zhang, H. Liu, K. Wang, Signal-domain Kalman filtering: an approach for maneuvering target surveillance with wideband radar. Signal Process. **177**, 107724 (2020)
20. Y. Yang, H. Su, Q. Hu, S. Zhou, J. Huang, Centralized adaptive cfar detection with registration errors in multistatic radar. IEEE Trans. Aerosp. Electron. Syst. **54**(5), 2370–2382 (2018)
21. M. Sun, W. Liu, J. Liu, C. Hao, Rao and wald tests for target detection in coherent interference. IEEE Trans. Aerosp. Electron. Syst. (2021). https://doi.org/10.1109/TAES.2021.3122833
22. Y. Zhao, L. Zhang, J. Bo, H. Liu, Z. Li, Three-dimensional reconstruction for space targets with multistatic inverse synthetic aperture radar systems. EURASIP J. Adv. Signal Process. **2019**(1), 40 (2019)
23. Z. Hu, W. Wang, F. Dong, P. Huang, MIMO radar accurate 3-D imaging and motion parameter estimation for target with complex motions. *Sensors*, 19(18) (2019)
24. C. Rago, P. Willett, Y. Bar-Shalom, Censoring sensors: a low-communication-rate scheme for distributed detection. IEEE Trans. Aerosp. Electron. Syst. **32**(2), 554–568 (1996)
25. S. Appadwedula, V.V. Veeravalli, D.L. Jones, Decentralized detection with censoring sensors. IEEE Trans. Signal Process. **56**(4), 1362–1373 (2008)
26. M. Scharrenbroich, M. Zatman, R. Balan, Performance of a practical two-step detector for non-fluctuating targets, in *2012 IEEE 7th Sensor Array and Multichannel Signal Processing Workshop (SAM)*, pp. 313–316 (2012)

27. M.A. Richards, *Fundamentals of Radar Signal Processing*, 2nd edn. (McGraw-Hill, New York, 2005)
28. M. Elhoseny, A. Tharwat, A.E. Hassanien, Bezier curve based path planning in a dynamic field using modified genetic algorithm. J. Computat. Sci. **25**, 339–350 (2018)
29. B.-S. Chen, B.-K. Lee, S.-C. Peng, Maximum likelihood parameter estimation of F-ARIMA processes using the genetic algorithm in the frequency domain. IEEE Trans. Signal Process. **50**(9), 2208–2220 (2002)
30. R.E. Kalman, A new approach to linear filtering and prediction problems. J. Basic Eng. **82D**, 35–45 (1960)
31. Y. Bar-Shalom, T. Kirubarajan, X. Rong Li, *Estimation with Applications to Tracking and Navigation* (Wiley, Hoboken, 2001)
32. S. Chen, Y. Xu, M. Zhu, K nearest neighbor joint possibility data association algorithm, in *2010 2nd International Conference on Information Engineering and Computer Science*, pp. 1–4 (2010)

Publisher's Note